

## The X-ray Link Between High Eddington Ratio Dust-Obscured Galaxies (DOGs) and Hot DOGs

FAN ZOU <sup>1</sup>, W. N. BRANDT <sup>2,3,4</sup>, ELENA GALLO <sup>1</sup>, FABIO VITO <sup>5</sup> AND ZHIBO YU <sup>2,3</sup>

<sup>1</sup>Department of Astronomy, University of Michigan, 1085 S University, Ann Arbor, MI 48109, USA

<sup>2</sup>Department of Astronomy and Astrophysics, 525 Davey Lab, The Pennsylvania State University, University Park, PA 16802, USA

<sup>3</sup>Institute for Gravitation and the Cosmos, The Pennsylvania State University, University Park, PA 16802, USA

<sup>4</sup>Department of Physics, 104 Davey Laboratory, The Pennsylvania State University, University Park, PA 16802, USA

<sup>5</sup>INAF – Osservatorio di Astrofisica e Scienza dello Spazio di Bologna, Via Gobetti 93/3, 40129 Bologna, Italy

### ABSTRACT

Dust-obscured galaxies (DOGs) with extremely red optical-to-infrared colors are often associated with intense starburst and AGN activity. Studying DOGs can provide insights into the processes that drive the growth of galaxies and their central supermassive black holes. However, the general DOG population is heterogeneous, spanning a wide range of evolutionary stages, and has X-ray obscuring column densities ( $N_{\text{H}}$ ) covering low-to-high levels. In this work, we focus on seven **high Eddington ratio DOGs** ( $\log \lambda_{\text{Edd}} \gtrsim -0.5$ ) to examine their X-ray obscuration properties using new and archival X-ray observations. We confirm that these systems are generally heavily obscured, with 6/7 having  $N_{\text{H}} \gtrsim 10^{23} \text{ cm}^{-2}$  and 3/7 having  $N_{\text{H}} \gtrsim 10^{24} \text{ cm}^{-2}$ . Based on the observed similarity with the rare Hot DOG population, we argue that both high- $\lambda_{\text{Edd}}$  DOGs and Hot DOGs likely trace the post-merger phase during which AGNs are enshrouded by large columns of dust-rich material.

**Keywords:** Active galactic nuclei (16) — Galaxy evolution (594) — AGN host galaxies (2017)

### 1. INTRODUCTION

Within the coevolution framework of supermassive black holes (SMBHs) and their host galaxies (e.g., D. B. Sanders et al. 1988; P. F. Hopkins et al. 2006, 2008; D. M. Alexander & R. C. Hickox 2012), major mergers of gas-rich galaxies can trigger intense starburst activity and drive material toward the central SMBHs, fueling accretion. The peak activity of both SMBH accretion and star formation occurs during dust-enshrouded, heavily obscured phases, with the (obscured) SMBH accretion approaching the Eddington limit (e.g., D. Narayanan et al. 2010; E. Treister et al. 2010; G. B. Lansbury et al. 2015; F. Vito et al. 2018). Subsequently, radiation-driven outflows from near the central SMBH sweep away the obscuring material (“blow-out” phase; e.g., P. F. Hopkins & M. Elvis 2010; A. C. Fabian 2012 and references therein), allowing the SMBH to manifest as an unobscured active galactic nucleus (AGN).

Hot dust-obscured galaxies (Hot DOGs) and DOGs have been suggested to represent key post-merger evolutionary phases. Both are selected observationally for their extremely red optical and/or infrared (IR) colors (A. Dey et al. 2008; P. R. M. Eisenhardt et al. 2012; Y. Toba & T. Nagao 2016; Y. Toba et al. 2017; J. Wu et al. 2012, 2018), potentially

representing the peak phase of SMBH accretion, AGN obscuration, and host star formation in the coevolution framework. Hot DOGs are detected by Wide-field Infrared Survey Explorer (WISE) at 12 and 22  $\mu\text{m}$ , but nearly undetected at 3.4 and 4.6  $\mu\text{m}$  (P. R. M. Eisenhardt et al. 2012; J. Wu et al. 2012). They are a rare population with a sky surface density of approximately one candidate per 30  $\text{deg}^2$  and are thought to be primarily powered by deeply buried, massive SMBHs with high Eddington ratios ( $\lambda_{\text{Edd}}$ ). Their extreme optical/IR colors are thought to result from emission by hot dust, reaching temperatures up to hundreds of K, heated by central SMBHs (e.g., C.-W. Tsai et al. 2015; J. Wu et al. 2018; G. Li et al. 2024).

DOGs are typically selected with 24  $\mu\text{m}$  fluxes  $f_{24 \mu\text{m}} \geq 0.3 \text{ mJy}$  and  $R$ -band to 24  $\mu\text{m}$  colors  $(R - [24])_{\text{Vega}} \geq 14$  (A. Dey et al. 2008). Y. Toba & T. Nagao (2016) additionally applied a criterion of  $f_{22 \mu\text{m}} \geq 3.8 \text{ mJy}$  and  $i - [22] \geq 7$  to select IR-bright DOGs, which tend to have larger AGN contributions. DOGs are generally less extreme, characterized by less-massive SMBHs and larger host-galaxy contributions, and they have smaller intrinsic 2 – 10 keV luminosities ( $L_{\text{X}}$ ) compared to the rarer Hot DOGs. Compared to Hot DOGs, DOGs are more common and representative in the Universe. Numerically, the surface number density of DOGs on the sky can reach  $\approx 300 \text{ deg}^{-2}$  in deep fields (e.g., A. Dey et al. 2008; Z. Yu et al. 2024), but the surface num-

ber density of Hot DOGs is four orders of magnitude lower ( $\approx 0.03 \text{ deg}^{-2}$ ; P. R. M. Eisenhardt et al. 2012; J. Wu et al. 2012).

X-ray observations provide unique insights into the nature of (Hot) DOGs. One of the primary advantages of X-rays is their high penetration power, which enables the direct identification of AGNs buried in large column densities ( $N_{\text{H}}$ ) of obscuring material. Studies have found that Hot DOGs exhibit high  $L_{\text{X}}$  with nearly Compton-thick obscuration (D. Stern et al. 2014; R. J. Assef et al. 2016, 2020; C. Ricci et al. 2017a; F. Vito et al. 2018; L. Zappacosta et al. 2018). Notably, F. Vito et al. (2018) concluded that Hot DOGs occupy a distinct region in the  $N_{\text{H}} - L_{\text{X}}$  plane, characterized by much higher  $N_{\text{H}}$  than luminous red type 1 quasars, which are thought to be transitioning from a heavily obscured phase to an unobscured blue-quasar phase.

However, the X-ray obscuration of DOGs spans a wider  $N_{\text{H}}$  range than that of Hot DOGs (G. Lanzuisi et al. 2009; A. Corral et al. 2016; L. A. Riguccini et al. 2019; N. Cristello et al. 2024; A. Kayal & V. Singh 2024; Z. Yu et al. 2024). This suggests that the DOG population may be heterogeneous, potentially covering a wide range of evolutionary stages or even sometimes be explained by episodes of star formation, as concluded in Z. Yu et al. (2024) based on studying a large sample of well-characterized DOGs. Z. Yu et al. (2024) also demonstrated that the general DOG population is not primarily driven by major mergers and that typical AGN-containing DOGs are analogous to extreme type 2 AGNs instead of Hot DOGs. However, F. Zou et al. (2020) argued that high- $\lambda_{\text{Edd}}$  DOGs naturally tend to be close to the dust-enshrouded phase after major mergers and, like Hot DOGs, are likely heavily obscured in X-rays. We note that previously identified DOG samples rarely reach  $N_{\text{H}} \gtrsim 10^{23.5} \text{ cm}^{-2}$ , implying that heavily obscured DOGs (i.e., the analogs of Hot DOGs) may be severely underrepresented. The few reported heavily obscured DOGs (e.g., Y. Toba et al. 2020; F. Zou et al. 2020; N. Cristello et al. 2024) indeed also have high  $\lambda_{\text{Edd}}$ .

To further constrain the X-ray obscuration levels of high- $\lambda_{\text{Edd}}$  DOGs, we compile seven DOGs with known high  $\lambda_{\text{Edd}}$  values that are comparable to those of Hot DOGs (generally having  $-0.5 \lesssim \log \lambda_{\text{Edd}} \lesssim 0.5$ ; e.g., G. Li et al. 2024) and target four of them with Chandra observations in this work. The detailed sample selection will be presented in Section 2. We will probe if our sources are indeed heavily obscured, as has been seen for Hot DOGs, in Section 3. We adopt a flat  $\Lambda$ CDM cosmology with  $H_0 = 70 \text{ km s}^{-1} \text{ Mpc}^{-1}$ ,  $\Omega_{\Lambda} = 0.7$ , and  $\Omega_M = 0.3$ . For simplicity, we will write SDSS Jhhmmss.ss±ddmmss.s as Jhhmm±ddmm in the main text. We will use  $L_{\text{X}}$  and  $L_{\text{X,obs}}$  to represent intrinsic and observed (i.e., without absorption corrections) 2–10 keV luminosities,

respectively, unless otherwise noted. We will always adopt  $\text{cm}^{-2}$  as the unit of  $N_{\text{H}}$ .

## 2. SAMPLE SELECTION

Our sample is primarily drawn from the high- $\lambda_{\text{Edd}}$  DOG sample in F. Zou et al. (2020), which was initially from Y. Toba & T. Nagao (2016) and Y. Toba et al. (2017). Y. Toba et al. (2017) systematically selected 36 IR-bright DOGs with  $(i-[22])_{\text{AB}} > 7$ ,  $22 \mu\text{m}$  flux densities above 3.8 mJy, and clear [O III] from the Sloan Digital Sky Survey. Among them, F. Zou et al. (2020) further selected sources with broad Mg II or H $\beta$  lines and targeted 12 DOGs with Cycle 20 Chandra snapshot observations ( $\approx 3$  ks per source). The goal of selecting broad-line DOGs is to measure their black-hole masses ( $M_{\text{BH}}$ ), and, consequently,  $\lambda_{\text{Edd}}$ , based on their broad-line widths by assuming a virial equilibrium in the broad-line region. Measuring  $M_{\text{BH}}$  also requires intrinsic, deabsorbed AGN optical or UV luminosities (e.g., Y. Shen 2013). These were derived from SED fitting by recovering the deabsorbed AGN SED components, as has been done in F. Zou et al. (2020), and such techniques have also been implemented to measure  $M_{\text{BH}}$  values for Hot DOGs (e.g., G. Li et al. 2024). F. Zou et al. (2020) showed that these 12 DOGs generally have high  $\lambda_{\text{Edd}}$  and utilized Cycle 20 Chandra observations to examine their basic X-ray obscuration properties. All three targets with  $\lambda_{\text{Edd}} < 0.1$  were X-ray-detected, but only 3 out of 9 sources with  $\lambda_{\text{Edd}} > 0.1$  were detected. At least at face value, the lower detection rates at higher  $\lambda_{\text{Edd}}$  may suggest that high- $\lambda_{\text{Edd}}$  DOGs are more obscured. However, the short Chandra exposures in F. Zou et al. (2020) hindered more effective constraints on the X-ray absorption columns of high- $\lambda_{\text{Edd}}$  DOGs.

To further improve the constraints on high- $\lambda_{\text{Edd}}$  DOGs, we conducted follow-up X-ray observations with longer exposure. Given our available follow-up resources, we focus on the six DOGs with the higher half of  $\lambda_{\text{Edd}}$  in the sample of F. Zou et al. (2020) ( $\log \lambda_{\text{Edd}} \gtrsim -0.5$ ) as they are more representative of the extreme high- $\lambda_{\text{Edd}}$  DOG population. As shown in G. Li et al. (2024), the  $\lambda_{\text{Edd}}$  of Hot DOGs is mainly distributed across  $-0.5 \lesssim \log \lambda_{\text{Edd}} \lesssim 0.5$  (see their Figures 6 and 7), and thus DOGs below  $\log \lambda_{\text{Edd}} \lesssim -0.5$  in F. Zou et al. (2020) are not formally high- $\lambda_{\text{Edd}}$  DOGs with  $\lambda_{\text{Edd}}$  comparable to Hot DOGs. Besides, we do not have new observations of these lower- $\lambda_{\text{Edd}}$  DOGs and thus do not have effective constraints on their  $N_{\text{H}}$ . Therefore, the remaining DOGs with lower  $\lambda_{\text{Edd}}$  in F. Zou et al. (2020) will not be discussed in this work.

We have obtained a 68 ks follow-up XMM-Newton observation for the X-ray brightest source in the sample, J1324+4501, confirming its heavily obscured nature with  $\log N_{\text{H}} = 23.43^{+0.09}_{-0.13}$  (N. Cristello et al. 2024). In this work, we obtained longer Cycle 25 Chandra exposures ( $\approx 15$  ks

per source) for the four fainter sources, where the exposures are set to ensure that, even if these sources are undetected, the corresponding X-ray upper limits are sufficiently tight to confirm the heavily obscured nature. This work presents the new Chandra observations and combines these newly observed sources with the archival ones to provide constraints on the X-ray obscuration levels of high- $\lambda_{\text{Edd}}$  DOGs.

Besides the six high- $\lambda_{\text{Edd}}$  DOGs from F. Zou et al. (2020), we also supplement the sample with the single source, J0825+3002, reported in Y. Toba et al. (2020). This DOG was also from the initial IR-bright DOG sample in Y. Toba & T. Nagao (2016) and observed by XMM-Newton and NuSTAR, showing a Compton-thick  $N_{\text{H}} = 1.0^{+0.8}_{-0.4} \times 10^{24} \text{ cm}^{-2}$ . Y. Toba et al. (2020) estimated its  $M_{\text{BH}}$  based on the scaling relation between  $M_{\text{BH}}$  and host-galaxy stellar mass, which places J0825+3002 to also be a high- $\lambda_{\text{Edd}}$  DOG with  $\lambda_{\text{Edd}} = 0.7$ . Although this  $\lambda_{\text{Edd}}$  measurement is indirect, we include this source for completeness. We note that explicitly reported high- $\lambda_{\text{Edd}}$  DOGs are rare because it is generally challenging to confirm their high  $\lambda_{\text{Edd}}$ . We include both samples in Y. Toba et al. (2020) and F. Zou et al. (2020) to represent the best knowledge we have regarding this population. Removing J0825+3002 out of our sample would not materially affect our overall conclusions in Section 4.

We summarize the properties of our sources in Table 1. The X-ray properties are either from the literature (the last three rows of the table) or will be derived in Section 3.2 (the first four rows of the table). For sources other than J0825+3002, the  $M_{\text{BH}}$  and  $\lambda_{\text{Edd}}$  are from Table 4 in F. Zou et al. (2020) and are all derived from broad Mg II lines. For J0825+3002, its  $M_{\text{BH}}$  is based on the scaled host stellar mass, as reported in Section 3.3 of Y. Toba et al. (2020).

Although the statistical  $\lambda_{\text{Edd}}$  uncertainties may not allow a firm conclusion on  $\log \lambda_{\text{Edd}} > -0.5$  for individual sources, they are sufficiently small to prove that our sample as a whole can represent high- $\lambda_{\text{Edd}}$  DOGs – if adopting 0.5 dex as the nominal uncertainty for J0825+3002’s  $\log \lambda_{\text{Edd}}$ , the uncertainty of the weighted arithmetic mean  $\log \lambda_{\text{Edd}}$  of our sample would be only 0.06. However, systematic uncertainties are not directly considered here and may be more prominent. The most relevant uncertainty is the viability of using broad lines to infer  $M_{\text{BH}}$  for DOGs. In fact, the origin of the broad lines in such heavily X-ray obscured systems has been under continuous investigation. Relevantly, it is not uncommon for Hot DOGs to show broad lines (C.-W. Tsai et al. 2018; J. Wu et al. 2018; L. Finnerty et al. 2020; H. D. Jun et al. 2020; G. Li et al. 2024). The broad lines of some Hot DOGs are suggested to be potentially from outflows instead of the broad-line region (e.g. L. Finnerty et al. 2020; H. D. Jun et al. 2020). However, follow-up studies of a subpopulation of Hot DOGs that show significant excess blue emission (R. J. Assef et al. 2016, 2020, 2022) revealed that the

blue emission and their broad lines should be the scattered light from central AGNs based on, e.g., multiwavelength and polarimetry observations. G. Li et al. (2024) further argued that, for general Hot DOGs, their broad lines may also be mainly scattered emission, and hence these broad lines can be used to estimate  $M_{\text{BH}}$ . For our DOGs specifically, F. Zou et al. (2020) showed that their broad Mg II line profiles are generally different from the outflow [O III] profiles (see their Section 5.2 for more discussion). Therefore, the broad lines of our sources are highly likely also from scattered emission from the broad-line regions. Nevertheless, an outflow origin cannot be deterministically ruled out, and this is a fundamental caveat for not only our DOGs but also all the Hot DOGs and relevant works in general.

### 3. DATA AND RESULTS

In this section, we will first present the new Chandra observations (Section 3.1) and  $N_{\text{H}}$  constraints (Section 3.2) for four sources in our sample and then combine them with the remaining three archival sources in our sample to discuss the implications for high- $\lambda_{\text{Edd}}$  DOGs (Section 3.3).

#### 3.1. Chandra Data Reduction

The four sources with new Chandra Cycle 25 observations also have Cycle 20 observations; we summarize them all in Table 2. The data were reduced using CIAO 4.16 and CALDB 4.11.2. We first run the `chandra_repro` script with the option `check_vf_pha = yes` since our observations were taken in Very Faint mode. We then use the `fluximage` script to generate images with weights according to a redshifted absorbed power-law model, where the redshift is set to the known value, the intrinsic  $N_{\text{H}}$  is set to  $10^{24} \text{ cm}^{-2}$ , and the photon index is set to  $\Gamma = 2$ . The weighting parameters are based on prior estimates indicating that our sources are highly obscured. Their exact values are not critical, and altering them does not affect the results. We further use the `specextract` script to extract X-ray spectra, grouped to at least one count per bin, and response files with  $2''$  circular source regions and annulus background regions with inner and outer radii of  $10''$  and  $40''$  centered at the source position. As shown in Table 2, there is no apparent count-rate variability between the Cycle 20 and Cycle 25 observations, and we will jointly analyze them hereafter.

To assess whether the sources are detected, we calculate the binomial no-source probability  $P_B$  (P. S. Broos et al. 2007; M. C. Weisskopf et al. 2007). We set a detection threshold of  $P_B = 0.01$ , suitable for sources with known locations. By combining data from Cycle 20 and Cycle 25 observations, we successfully detected J1210+6105 (3 source-region counts) and J1235+4827 (17 source-region counts), with  $P_B = 1 \times 10^{-3}$  and  $2 \times 10^{-26}$ , respectively; J1042+2451 and J1513+1451 are not detected.

**Table 1.** Source Properties.

SDSS Name	$z$	$\log M_{\text{BH}}$ ( $M_{\odot}$ )	$\log \lambda_{\text{Edd}}$	$\log L_{\text{X,obs}}$ ( $\text{erg s}^{-1}$ )	$\log L_{\text{X}}$ ( $\text{erg s}^{-1}$ )	$\log N_{\text{H}}$ ( $\text{cm}^{-2}$ )
(1)	(2)	(3)	(4)	(5)	(6)	(7)
J104241.10+245107.0	1.026	$8.80 \pm 0.15$	$-0.48 \pm 0.16$	$< 42.8$	$44.4^{+0.3}_{-0.4}$	$> 24.0$
J121056.92+610551.5	0.926	$7.89 \pm 0.33$	$-0.11 \pm 0.35$	$42.5^{+0.3}_{-0.2}$	$43.6^{+0.8}_{-0.4}$	$23.3^{+1.6}_{-0.9}$
J123544.97+482715.4	1.023	$8.20 \pm 0.12$	$-0.60 \pm 0.08$	$43.4^{+0.1}_{-0.1}$	$43.8^{+0.1}_{-0.1}$	$< 22.5$
J151354.48+145125.2	0.882	$8.15 \pm 0.12$	$-0.33 \pm 0.16$	$< 42.5$	$44.1^{+0.3}_{-0.5}$	$> 23.9$
J082501.48+300257.1*	0.890	$8.40^a$	$-0.15^a$	44.1	$44.6^{+0.2}_{-0.2}$	$24.0^{+0.3}_{-0.2}$
J132440.17+450133.8*	0.774	$8.27 \pm 0.40$	$-0.06 \pm 0.40$	$44.11^{+0.05}_{-0.04}$	$44.71^{+0.08}_{-0.12}$	$23.43^{+0.09}_{-0.13}$
J152504.74+123401.7*	0.851	$8.36 \pm 0.23$	$-0.51 \pm 0.24$	$43.3^{+0.2}_{-0.2}$	$44.3^{+0.3}_{-0.3}$	$23.2^{+0.3}_{-0.3}$

*Notes.* (2) Redshifts. All quoted redshifts are spectroscopic, except for J0825+3002, which only has a photometric redshift. (3) Black-hole masses. (4) Eddington ratios. (5) 2 – 10 keV luminosities without absorption corrections. (6) Intrinsic (unabsorbed) 2–10 keV luminosities. For J1042+2451, J1210+6105, and J1513+1451, these measurements are primarily set by the prior instead of the X-ray data. (7) Intrinsic line-of-sight hydrogen-equivalent column densities. The confidence intervals of the measured values represent 68% levels, while the limits are at a 95% level.

\* X-ray measurements for J0825+3002, J1324+4501, and J1525+1234 are from [Y. Toba et al. \(2020\)](#), [N. Cristello et al. \(2024\)](#), and [F. Zou et al. \(2020\)](#), respectively.

<sup>a</sup> The  $M_{\text{BH}}$  of J0825+3002 is estimated based on the scaling relation between  $M_{\text{BH}}$  and the host stellar mass. Therefore, its  $M_{\text{BH}}$  and  $\lambda_{\text{Edd}}$  have nominal uncertainties of  $\approx 0.5$  dex from the scaling relation.

**Table 2.** X-ray Observation Logs.

SDSS Name	ObsID	Date (yyyy-mm-dd)	Exposure Time (ks)	Counts	Net counts
(1)	(2)	(3)	(4)	(5)	(6)
J104241.10+245107.0	21143	2018-11-16	3.1	1	$< 4.7$
	28791	2024-05-04	15.4	0	
J121056.92+610551.5	21141	2018-12-24	3.1	0	$2.8^{+2.9}_{-0.9}$
	28789	2024-04-07	15.4	3	
J123544.97+482715.4	21140	2018-11-06	2.9	2	$16.8^{+5.2}_{-3.2}$
	28792	2024-11-19	14.4	15	
J151354.48+145125.2	21145	2018-12-26	3.1	0	$< 3.1$
	28790	2024-09-15	15.4	0	

*Notes.* (1) SDSS positions in Jhhmmss.ss±ddmmss.s. (2) Chandra observation IDs. (3) Observation starting date. (4) Exposure time. (5) Total counts within 2". (6) Target net counts combining both observations.

We further constrain the expected net source counts within the source apertures using the method described in Appendix A of [M. C. Weisskopf et al. \(2007\)](#). The 68% confidence intervals for the counts of detected sources and the 95% upper limits for undetected sources are presented in Table 2.

### 3.2. $N_{\text{H}}$ Measurements

We convert the net counts to  $L_{\text{X,obs}}$  using a power-law model with  $\Gamma = 1.4$  and the extracted Chandra response files. Figure 1 illustrates the comparison between  $L_{\text{X,obs}}$  and the AGN 6  $\mu\text{m}$  luminosities,  $L_{6\mu\text{m}} = \nu L_{\nu}(6\mu\text{m})$ , for the entire sample. The  $L_{6\mu\text{m}}$  values were estimated by [Y.](#)

[Toba et al. \(2020\)](#) and [F. Zou et al. \(2020\)](#) by decomposing the corresponding spectral energy distributions (SEDs). The three archival sources (J0825+3002, J1324+4501, and J1525+1234) have reported intrinsic, deabsorbed 2 – 10 keV luminosities  $L_{\text{X}}$  ([Y. Toba et al. 2020](#); [F. Zou et al. 2020](#); [N. Cristello et al. 2024](#)). With our new observations, J1235+4827 also has sufficient counts to allow basic  $L_{\text{X}}$  measurements (see the latter part of this section). Therefore, we also plot intrinsic  $L_{\text{X}}$  values for these four sources in the figure. For comparison, we display the expected AGN  $L_{\text{X}} - L_{6\mu\text{m}}$  relation from [D. Stern \(2015\)](#) and  $L_{\text{X}}$  of typical DOGs reported by [A. Corral et al. \(2016\)](#) and [Z. Yu et al. \(2024\)](#). The goal of presenting intrinsic  $L_{\text{X}}$  instead of  $L_{\text{X,obs}}$

for these typical DOGs is to help evaluate if DOGs follow the AGN  $L_X - L_{6\mu\text{m}}$  relation. The relation in [D. Stern \(2015\)](#) was empirically constructed for typical AGNs and was shown to be applicable over six orders of magnitude in  $L_X$ . Those AGNs with  $L_{X,\text{obs}}$  significantly below the relation may have X-ray emission suppressed by heavy obscuration. For visual guidance, we also plot the expected suppressed  $L_{X,\text{obs}} - L_{6\mu\text{m}}$  relation when  $N_{\text{H}} = 10^{24} \text{ cm}^{-2}$  in the figure, i.e., moving the original  $L_X - L_{6\mu\text{m}}$  relation downward by 1.5 dex.

The  $L_X$  values of typical DOGs generally align with the expected relation. Similarly, for the plotted four DOGs with  $L_X$  measurements in our sample, their  $L_X$  values also agree well with the expected relation. However, all the  $L_{X,\text{obs}}$  of our DOGs fall significantly below this relation, suggesting that their X-ray emission may be heavily suppressed by strong obscuration. Strictly speaking, the suppressed  $L_{X,\text{obs}}$  might also be explained by intrinsic X-ray weakness, but we argue that this is not a preferred explanation. As shown in [Figure 1](#), there is no ambiguity that both general DOGs and 4/7 of our sources are not significantly intrinsically X-ray weak. Regarding the three remaining sources (J1042+2451, J1210+6105, and J1513+1451), their  $L_{X,\text{obs}}$  values are over two dex below the  $L_X - L_{6\mu\text{m}}$  relation. Even if our high- $\lambda_{\text{Edd}}$  DOGs can be argued to be different from general DOGs but instead more like Hot DOGs, such a large weakness, if intrinsic, is still not expected by making an analogy to Hot DOGs. Hot DOGs present at most moderate intrinsic X-ray weakness in previous works. [F. Vito et al. \(2018\)](#) found that, on average, Hot DOGs may be slightly systematically below the  $L_X - L_{6\mu\text{m}}$  relation by 0.2 dex, while [C. Ricci et al. \(2017a\)](#) showed a somewhat larger suppression of 0.5 dex.<sup>6</sup> These differences are far from being sufficient to explain the suppressed  $L_{X,\text{obs}}$  by  $> 2$  dex for J1042+2451, J1210+6105, and J1513+1451. Therefore, we will primarily focus on the heavy-obscuration explanation in the following text.

It is important to highlight that all of our sources, regardless of detection status, are unlikely to be solely attributed to starburst activity in the absence of AGN emission, and the AGN signatures exist in both the optical and mid-IR bands. As shown in [Y. Toba et al. \(2017\)](#), these sources have broad Mg II lines and have high [O III]/H $\beta$  ratios (e.g., see [Figure 12](#) in [Y. Toba et al. \(2017\)](#)) that are characteristics of AGNs. Besides, the mid-IR colors of our sources from the WISE bands,  $W1 - W2$ , are all above 1.4 mag in the Vega system. Such red colors are above the AGN mid-IR color selection criterion,  $W1 - W2 \geq 0.8$ , in [D. Stern et al. \(2012\)](#) and are expected

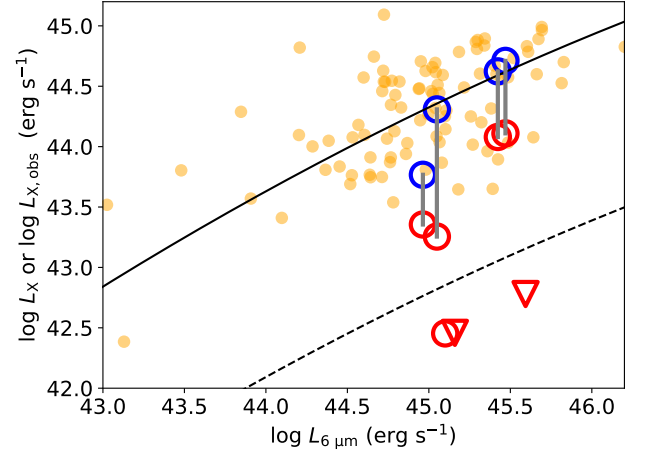


**Figure 1.**  $L_X$  vs.  $L_{6\mu\text{m}}$  for our sample, in larger open circles [downward triangles] representing detected [undetected] sources, and for the DOG sample of [A. Corral et al. \(2016\)](#) and [Z. Yu et al. \(2024\)](#), shown as orange filled circles. The red open circles or triangles represent  $L_{X,\text{obs}}$  for all of our sources, while the blue circles represent  $L_X$  for 4/7 of them; red and blue circles for the same sources are connected with vertical gray lines. All the orange circles are for  $L_X$ . These orange circles are mostly not heavily obscured, and thus their intrinsic  $L_X$  and  $L_{X,\text{obs}}$  only differ slightly, with a median offset of 0.2 dex. For comparison, the relation derived by [D. Stern \(2015\)](#) is shown as a solid black line, whereas the dashed black line illustrates the extent to which the relation is suppressed if  $N_{\text{H}} = 10^{24} \text{ cm}^{-2}$ . The  $L_X$  values of general DOGs and those in our sample are consistent with the AGN  $L_X - L_{6\mu\text{m}}$  relation. The  $L_{X,\text{obs}}$  values of our sample, on the other hand, are strongly suppressed compared to the relation, possibly indicating heavy X-ray obscuration.

to be from AGN SEDs because AGNs are much redder than galaxies in the mid-IR. [Figure 3](#) in [F. Zou et al. \(2020\)](#) also showed that strong AGN components are present in the mid-IR.

With the limited number of counts, we cannot simultaneously constrain  $L_X$  and  $N_{\text{H}}$  for the newly observed sources. Therefore, we focus on measuring  $N_{\text{H}}$  under the assumption that our sources follow the  $L_X - L_{6\mu\text{m}}$  relation within a reasonable scatter. The spectral analyses are conducted with BXA ([J. Buchner et al. 2014](#)) and Sherpa ([A. Siemiginowska et al. 2024](#)); the spectra are modeled with `phabs*(borus01+zphabs*cabs*cutoffpl)`, where `phabs` represents the Galactic absorption, `borus01` is the reprocessed spherical torus emission model of [M. Baloković et al. \(2018\)](#), `zphabs*cabs` models the source intrinsic absorption with Compton-scattering losses, and `cutoffpl` models the X-ray continuum. Since our sources may be in the dust-enshrouded phase, it is appropriate to adopt a covering factor of unity for the `borus01` model. Note that the `borus01` component only becomes important when  $N_{\text{H}} \gg 10^{24} \text{ cm}^{-2}$ , and thus its detailed geometry has little impact on the qualitative inference of the heavy-obscuration nature of

<sup>6</sup> Most of the obscuration corrections in [C. Ricci et al. \(2017a\)](#) are based on the scaling relation between the optical extinction and  $N_{\text{H}}$ , which has a large uncertainty, while the obscuration corrections in [F. Vito et al. \(2018\)](#) are directly based on X-ray data. Therefore, we regard the conclusion in [F. Vito et al. \(2018\)](#) to be more likely.

our sources. We fix the average  $N_{\text{H}}$  of the torus to  $10^{24} \text{ cm}^{-2}$  and use the inferred  $N_{\text{H}}$  values of `zphabs` and `cabs` to represent the line-of-sight  $N_{\text{H}}$ . We fix the `cutoffpl` power-law index and cut-off energy to  $\Gamma = 2$  and 500 keV, respectively. The two free parameters of the model are thus  $N_{\text{H}}$  and  $L_{\text{X}}$ . We adopt a flat prior for line-of-sight  $\log N_{\text{H}}$  within  $20 \leq \log N_{\text{H}} \leq 26$  and a normal prior for  $\log L_{\text{X}}$  centered at the  $L_{6 \mu\text{m}}$ -predicted values. The standard deviation ( $\approx 0.5$  dex) of the  $\log L_{\text{X}}$  prior accounts for the intrinsic scatter of the  $L_{\text{X}} - L_{6 \mu\text{m}}$  relation (0.4 dex) and the  $L_{6 \mu\text{m}}$  uncertainties. Note that we are not placing the assumed  $L_{\text{X}}$  exactly on the  $L_{\text{X}} - L_{6 \mu\text{m}}$  relation; instead, the prior dispersion still allows  $L_{\text{X}}$  to deviate away by one dex within the  $2\sigma$  range of the prior.

We deliberately adopted a physically motivated, weakly informative prior for  $L_{\text{X}}$  because, as mentioned earlier, we would like to measure how much the obscuration level needs to reach to explain the low  $L_{\text{X,obs}}$  if our sources follow the  $L_{\text{X}} - L_{6 \mu\text{m}}$  relation within a reasonable scatter. This is a both necessary and reasonable assumption. The necessity is based on the fact that our sources are limited in counts, and thus it is infeasible to simultaneously constrain  $L_{\text{X}}$  and  $N_{\text{H}}$  for, at least, J1042+2451, J1210+6105, and J1513+1451, which have less than three counts each. We can only constrain one of these two parameters (or their limits) after assuming the other one. Our adopted assumption is also reasonable. We have verified that both DOG samples in [A. Corral et al. \(2016\)](#) and [Z. Yu et al. \(2024\)](#) are in good consistency with our prior, as can be visually seen in [Figure 1](#) – both samples have a dispersion of 0.38 dex around the expected  $L_{\text{X}} - L_{6 \mu\text{m}}$  relation in [D. Stern \(2015\)](#) and a much smaller median offset. Besides, as shown in [Figure 1](#), the intrinsic  $L_{\text{X}}$  of 4/7 sources in our sample are in good consistency with the  $L_{\text{X}} - L_{6 \mu\text{m}}$  relation. As discussed earlier in this section, previous works also reported that both DOGs and Hot DOGs, either individually or as a sample, are not too far away from the  $L_{\text{X}} - L_{6 \mu\text{m}}$  relation (e.g., [C. Ricci et al. 2017a](#); [F. Vito et al. 2018](#); [L. Zappacosta et al. 2018](#); [Y. Toba et al. 2020](#); [N. Cristello et al. 2024](#); [Z. Yu et al. 2024](#)).

The sampling of the posterior probability distributions is conducted with `BXA`, which has internally implemented the nested sampling Monte Carlo algorithm in the `UltraNest` package, as presented in [J. Buchner \(2021\)](#). We integrate out  $L_{\text{X}}$  and show the sampled marginal line-of-sight  $N_{\text{H}}$  posterior distributions in [Figure 2](#). The  $N_{\text{H}}$  posterior of J1235+4827 has an apparent peak at  $\log N_{\text{H}} \approx 23.3$ . The posteriors of J1042+2451 and J1513+1451 are small at low  $N_{\text{H}}$  and reach plateaus at high  $N_{\text{H}}$ , and thus we can constrain their  $N_{\text{H}}$  lower limits. In contrast, J1235+4827 has an  $N_{\text{H}}$  upper limit. [Appendix A](#) also shows that the posteriors are generally robust against reasonable changes of the prior. These  $N_{\text{H}}$  measurements are reported in [Table 1](#) together with the

other three high- $\lambda_{\text{Edd}}$  DOGs (J0825+3002, J1324+4501, and J1525+1234) from [Y. Toba et al. \(2020\)](#), [F. Zou et al. \(2020\)](#), and [N. Cristello et al. \(2024\)](#). The X-ray spectra of these literature-reported DOGs generally have much higher constraining power, and thus their measurements will remain similar no matter if we apply the  $\log L_{\text{X}}$  prior to their data. [Table 1](#) indicates that most of our sources are heavily obscured, potentially reaching a Compton-thick level.

[Table 1](#) presents the inferred intrinsic  $L_{\text{X}}$ . The measurements for J1042+2451, J1210+6105, and J1513+1451 are influenced by the prior, which is evident from the large uncertainties in  $L_{\text{X}}$ . The intrinsic  $L_{\text{X}}$  values of the remaining sources better reflect the X-ray data constraints.

### 3.3. The $N_{\text{H}} - L_{\text{X}}$ and $N_{\text{H}} - \lambda_{\text{Edd}}$ Planes

We display all of our seven sources in the  $N_{\text{H}} - L_{\text{X}}$  plane in [Figure 3](#). For comparison, we also plot red type 1 quasars ([T. Urrutia et al. 2005](#); [S. Martocchia et al. 2017](#); [G. Mountrichas et al. 2017](#); [A. D. Goulding et al. 2018](#); [G. B. Lansbury et al. 2020](#)), Hot DOGs ([D. Stern et al. 2014](#); [R. J. Assef et al. 2016](#); [C. Ricci et al. 2017a](#); [F. Vito et al. 2018](#); [L. Zappacosta et al. 2018](#)), and DOGs ([G. Lanzuisi et al. 2009](#); [A. Corral et al. 2016](#); [Z. Yu et al. 2024](#)). Our sources have  $L_{\text{X}}$  values comparable to other DOGs, but they appear to be generally more obscured, with 6 out of 7 of our sample having  $N_{\text{H}} \gtrsim 10^{23} \text{ cm}^{-2}$ . Three of our sources—J0825+3002, J1042+2451, and J1513+1451—reside in the Compton-thick regime, a region that is largely unoccupied by other DOGs. Such a difference also exists between the higher-luminosity Hot DOGs versus red type 1 quasars, suggesting the possible physical link between high- $\lambda_{\text{Edd}}$  DOGs and Hot DOGs.

Furthermore, the  $N_{\text{H}} - \lambda_{\text{Edd}}$  plane also serves as a useful diagram relevant to AGN-driven outflows (e.g., [W. Ishibashi et al. 2018](#)). Recall that the classical Eddington limit is defined for pure ionized hydrogen and only includes the electron scattering cross-section. Real astronomical systems, however, usually have dusty gas instead, and dusts have a much higher overall absorption cross-section compared to gas. [A. C. Fabian et al. \(2006\)](#) introduced the term “effective Eddington limit” to account for the dust absorption cross section, where AGNs with effective Eddington limits above the unity are expected to generate outflows. As detailed in [W. Ishibashi et al. \(2018\)](#), the effective Eddington limit can be expressed as a function of  $\lambda_{\text{Edd}}$  and  $N_{\text{H}}$ , and the curve of an effective Eddington limit of unity divides the  $N_{\text{H}} - \lambda_{\text{Edd}}$  plane into a “forbidden region” (also known as the outflow region) and an “allowed region” (e.g., [D. Kakkad et al. 2016](#); [C. Ricci et al. 2017b](#); [W. Ishibashi et al. 2018, 2021](#)). Long-lived, obscuring clouds can only survive in the high- $N_{\text{H}}$  allowed region, where the obscuring material is sufficiently massive to withstand radiation pressure. [Figure 4](#) presents the two regions in the  $N_{\text{H}} - \lambda_{\text{Edd}}$  plane. The boundary be-

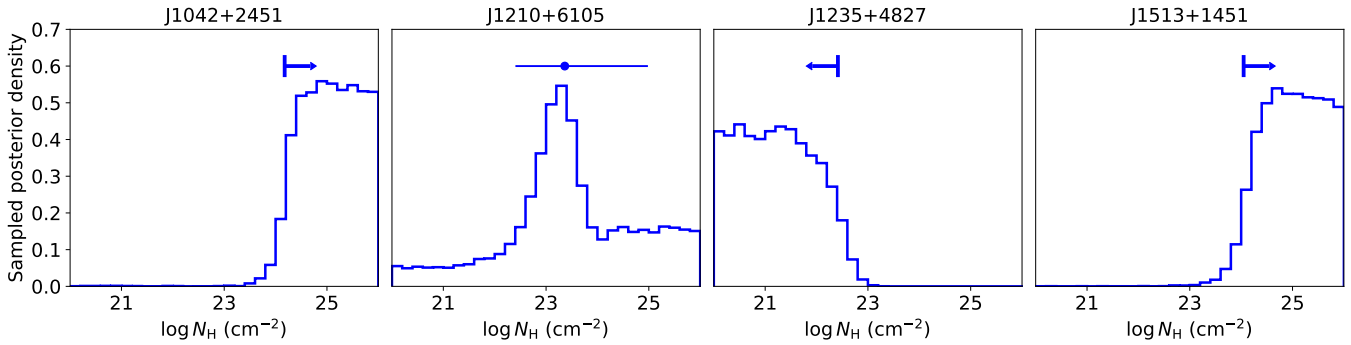


**Figure 2.** The sampled line-of-sight  $N_{\text{H}}$  posteriors of our newly observed sources. The rightward arrows for J1042+2451 and J1513+1451 represent 95% confidence lower limits, the leftward arrow for J1235+4827 represents a 95% confidence upper limit, and the point with a horizontal error bar for J1210+6105 represents the posterior median and 68% interval.

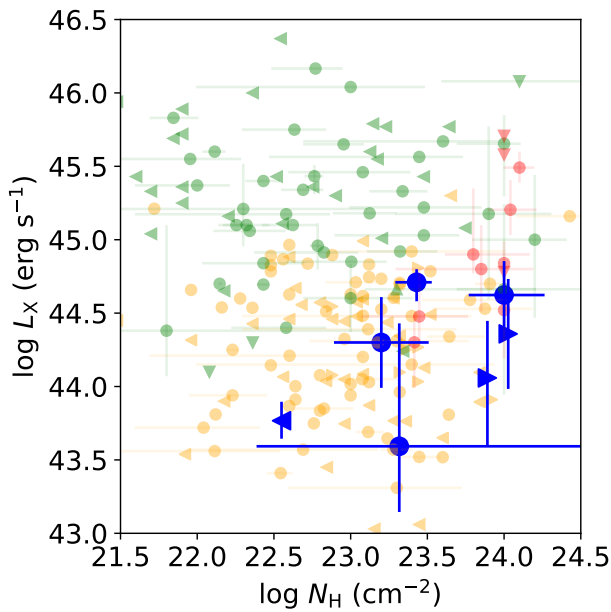


**Figure 3.** The  $N_{\text{H}} - L_{\text{X}}$  plane. Our sources are plotted as large blue circular points or triangles, where the leftward (rightward) triangles represent  $N_{\text{H}}$  upper (lower) limits. The green, orange, and red points are red type 1 quasars, DOGs, and Hot DOGs, respectively.

tween the two regions depends on the IR optical depth of the absorbing material (W. Ishibashi & A. C. Fabian 2015). In the single-scattering limit (i.e., the black solid curve in Figure 4), the medium is optically thick to UV but optically thin to IR such that UV photons are absorbed while reemitted IR photons would escape freely. In the radiation-trapping limit (i.e., the black dashed curve in Figure 4), the medium is optically thick to both UV and IR, and thus the reemitted IR photons would undergo multiple scatterings and exert larger momentum, leading to a larger forbidden region. Besides the medium in the vicinity of SMBHs, larger-scale dust lanes in their host galaxies may also cause some X-ray absorptions, but the corresponding  $N_{\text{H}}$  should be generally small. We fol-

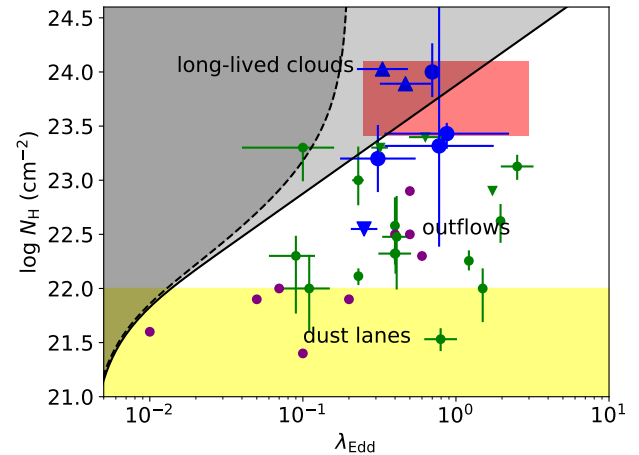


**Figure 4.** The  $N_{\text{H}} - \lambda_{\text{Edd}}$  plane. Our sources are plotted as large blue circular points or triangles, where the downward (upward) triangles represent  $N_{\text{H}}$  upper (lower) limits. The gray-shaded region is the allowed region for long-lived clouds, and the black solid (dashed) curves represent the boundaries between the allowed region and the outflow region at the single-scattering (radiation-trapping) limit (see W. Ishibashi et al. 2018 and further descriptions in Section 3.3). The yellow region represents obscuration possibly caused by host galaxies (C. Ricci et al. 2017b). The purple points are the sources with strong outflows, the green points represent red type 1 quasars, and the red shaded region is the expected region for Hot DOGs (C. Ricci et al. 2017a; F. Vito et al. 2018; J. Wu et al. 2018; G. Li et al. 2024).

low C. Ricci et al. (2017b) and W. Ishibashi et al. (2018) and adopt a nominal limit of  $N_{\text{H}} \leq 10^{22} \text{ cm}^{-2}$  (see Figure 3 in C. Ricci et al. 2017b) for the dust lanes (i.e., the yellow region in Figure 4).

We present our sources in the  $N_{\text{H}} - \lambda_{\text{Edd}}$  plane in Figure 4 together with sources with strong outflows (M. Brusa et al. 2015; D. Kakkad et al. 2016), red quasars (S. M. LaMassa et al. 2016, 2017; E. Glikman et al. 2017; G. B. Lansbury et al. 2020), and Hot DOGs (C. Ricci et al. 2017a; F. Vito et al. 2018; J. Wu et al. 2018; G. Li et al. 2024). Unlike AGNs

with strong outflows, our high- $\lambda_{\text{Edd}}$  DOGs and the Hot DOGs share a similar region in the  $N_{\text{H}}-\lambda_{\text{Edd}}$  plane and mainly reside at the boundary between the allowed region and the outflow region. Indeed, F. Zou et al. (2020) demonstrated that high- $\lambda_{\text{Edd}}$  DOGs exhibit only moderate outflows, characterized by outflow-broadened [O III] widths of  $\lesssim 1000 \text{ km s}^{-1}$ , which are narrower compared to sources with strong outflows (M. Brusa et al. 2015; G. B. Lansbury et al. 2020). From this, we conclude that both high- $\lambda_{\text{Edd}}$  DOGs and Hot DOGs are still in the process of entering the blow-out phase, during which strong AGN outflows start to expel the obscuring materials.

We note that J1235+4827, which has the smallest  $\lambda_{\text{Edd}}$  in our sample, is the only source that is not heavily obscured in X-rays. This source thus does not share the similarities with Hot DOGs and may not be in the dust-enshrouded phase after gas-rich galaxy mergers.

#### 4. SUMMARY

In this work, we present new Chandra observations of 4 high- $\lambda_{\text{Edd}}$  DOGs ( $\log \lambda_{\text{Edd}} \gtrsim -0.5$ ) and combine them with archival observations for 3 other high- $\lambda_{\text{Edd}}$  DOGs to probe their X-ray obscuration levels. We found that their  $L_{\text{X,obs}}$  all lie below the expected  $L_{\text{X}} - L_{6 \mu\text{m}}$  relation. Based on the prior knowledge that both DOGs and Hot DOGs are not strongly intrinsically X-ray weak, we argue that the low  $L_{\text{X,obs}}$  is caused by heavy obscuration. We further constrain the  $N_{\text{H}}$  with the inclusion of physically motivated  $\log L_{\text{X}}$  priors constructed based on the  $L_{\text{X}} - L_{6 \mu\text{m}}$  relation. We find that these systems are generally heavily obscured, with 6/7 having  $N_{\text{H}} \gtrsim 10^{23} \text{ cm}^{-2}$  and 3/7 having  $N_{\text{H}} \gtrsim 10^{24} \text{ cm}^{-2}$ .

Previous work (F. Zou et al. 2020) established that high- $\lambda_{\text{Edd}}$  DOGs share several important similarities with Hot DOGs: (i) their central SMBHs have high accretion rates; (ii) they are still entering the blow-out phase and do not have sufficiently strong outflows to sweep away large column densities of enshrouded materials; (iii) they are associated to intense host-galaxy starbursts. This work confirms that high- $\lambda_{\text{Edd}}$  DOGs, similar to Hot DOGs, are also heavily obscured in X-rays, potentially up to a Compton-thick level. These properties are consistent with the peak phase of AGN obscuration and SMBH and galaxy growth after gas-rich galaxy mergers and suggest that high- $\lambda_{\text{Edd}}$  DOGs and Hot DOGs are at similar evolutionary stages.

Nevertheless, as argued in previous works (e.g., Z. Yu et al. 2024), DOGs may originate from a heterogeneous popula-

tion that cannot always be explained by the merger-driven coevolution framework. In fact, Section 4.1 in Z. Yu et al. (2024) even showed that the fraction of DOGs hosting AGNs is similar to that of the typical matched galaxy population. Although the  $\lambda_{\text{Edd}}$  distribution of DOGs is still unknown, this may indicate that the majority of general DOGs do not have high  $\lambda_{\text{Edd}}$ . As Figure 3 shows, general DOGs span a wide range of  $N_{\text{H}}$  and are often not heavily obscured in X-rays. However, once we only focus on high- $\lambda_{\text{Edd}}$  DOGs, as represented by our sample, our results indicate that such sources would almost all populate in the heavily obscured regime. Therefore, our findings likely suggest that  $\lambda_{\text{Edd}}$  may be a key factor in distinguishing different types of DOGs. Within the DOG population, only those with high  $\lambda_{\text{Edd}}$  may serve as the less-massive analogs to Hot DOGs.

One of the main challenges in characterizing these sources is their low X-ray counts, which are a result of their high  $N_{\text{H}}$ . The limited counts may have hindered the X-ray identification of high- $\lambda_{\text{Edd}}$  DOGs in previous studies, and it is likely that those DOGs in the dust-enshrouded phase are still largely missed. With current X-ray facilities (e.g., Chandra and XMM-Newton), it would require several hundred kiloseconds per source to gather sufficient X-ray photons for detailed spectral analysis, making it a costly endeavor. Future X-ray observatories (e.g., Athena and AXIS) should offer much higher throughput, enabling better characterization of the dust-enshrouded, heavily obscured phase of merger-driven events.

#### ACKNOWLEDGMENTS

We thank the anonymous referee for constructive suggestions and comments. WNB acknowledges support from Chandra X-ray Center grant GO2-23083X and the Penn State Eberly Endowment. FV acknowledges support from the ‘‘INAF Ricerca Fondamentale 2023 – Large GO’’ grant. The Chandra ACIS team Guaranteed Time Observations utilized were selected by the ACIS Instrument Principal Investigator, Gordon P. Garmire, currently of the Huntingdon Institute for X-ray Astronomy, LLC. This paper employs a list of Chandra datasets, obtained by the Chandra X-ray Observatory, contained in DOI: 10.25574/cdc.417.

#### APPENDIX

##### A. TESTING DIFFERENT $\log L_{\text{X}}$ PRIORS

The main text assumes the  $\log L_{\text{X}}$  priors to center at the  $L_{6 \mu\text{m}}$ -predicted values. We also try shifting them downward by 0.5 dex to represent the fact that C. Ricci et al. (2017a) found a similar level of intrinsic X-ray weakness for Hot DOGs. This deviation

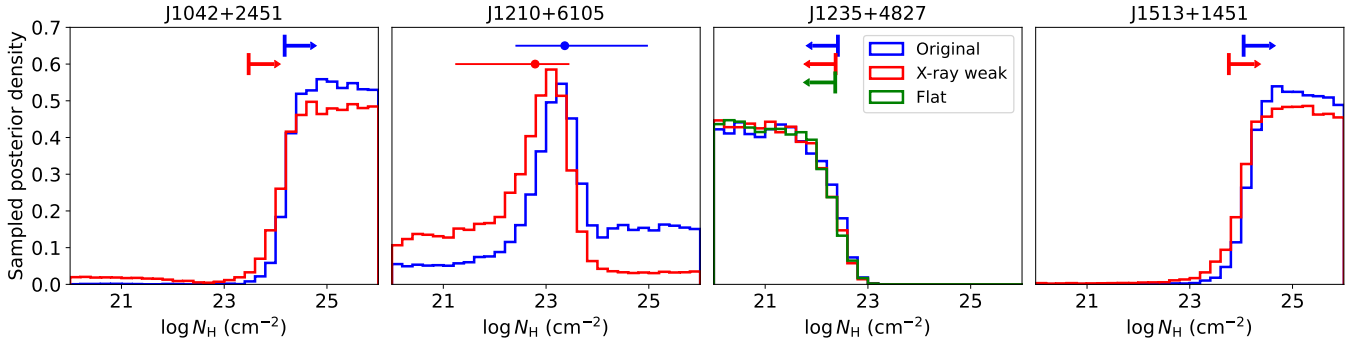


**Figure 5.** Comparison of the  $\log N_{\text{H}}$  posterior under different  $\log L_{\text{X}}$  prior choices. As labeled in the legend of the third panel, the blue histograms and the corresponding arrow limits (95% confidence) or error bars (68% confidence) are for the original results, i.e., the same as those in Figure 2; the red ones are based on the  $\log L_{\text{X}}$  priors systematically shifted downward by 0.5 dex; and the green one for J1235+4827 represents a flat  $\log L_{\text{X}}$  prior.

is already at an extreme level because F. Vito et al. (2018) showed that the intrinsic X-ray weakness of Hot DOGs may be milder (only 0.2 dex downward; see Footnote 6), and Figure 1 indicates that DOGs are generally not X-ray weak. Therefore, we do not move the priors down further because we want them to be still somewhat physically plausible. We conducted the same analyses as in Section 3.2 and compare the marginal  $\log N_{\text{H}}$  posterior in Figure 5. The figure shows that, even if this X-ray weak prior is adopted, the  $\log N_{\text{H}}$  posteriors remain largely similar, and the 95% lower limits of J1042+2451 and J1513+1451 are still above  $10^{23} \text{ cm}^{-2}$ . Our overall qualitative conclusions in the main text would not be affected.

J1235+4827 has many more counts than the other three sources (see Table 2). Therefore, it is feasible to further relax the assumption on the  $\log L_{\text{X}}$  prior. We tried a flat  $\log L_{\text{X}}$  prior and present the corresponding result in the third panel of Figure 5. The  $\log N_{\text{H}}$  posterior of J1235+4827 almost remains the same regardless of the prior choices, indicating that its inference is already data-dominated. We do not test a flat, noninformative prior for the other three sources because it would not provide any insights. For example, an extremely low  $\log L_{\text{X}}$  (even reaching  $-\infty$ ) would certainly be favoured for J1042+2451 and J1513+1451 because they do not have counts, but this case is physically unlikely. The necessity of a weakly informative prior instead of a noninformative prior for statistical inferences beyond the fully data-dominated regime is becoming more common in modern astronomy and should be considered useful instead of problematic, e.g., a notable example is that physical galaxy properties derived from SED fitting depend on priors and need a well-designed, physically motivated prior (e.g., A. de la Vega et al. 2025).

## REFERENCES

- Alexander, D. M., & Hickox, R. C. 2012, *NewAR*, 56, 93, doi: [10.1016/j.newar.2011.11.003](https://doi.org/10.1016/j.newar.2011.11.003)
- Assef, R. J., Walton, D. J., Brightman, M., et al. 2016, *ApJ*, 819, 111, doi: [10.3847/0004-637X/819/2/111](https://doi.org/10.3847/0004-637X/819/2/111)
- Assef, R. J., Brightman, M., Walton, D. J., et al. 2020, *ApJ*, 897, 112, doi: [10.3847/1538-4357/ab9814](https://doi.org/10.3847/1538-4357/ab9814)
- Assef, R. J., Bauer, F. E., Blain, A. W., et al. 2022, *ApJ*, 934, 101, doi: [10.3847/1538-4357/ac77fc](https://doi.org/10.3847/1538-4357/ac77fc)
- Baloković, M., Brightman, M., Harrison, F. A., et al. 2018, *ApJ*, 854, 42, doi: [10.3847/1538-4357/aaa7eb](https://doi.org/10.3847/1538-4357/aaa7eb)
- Broos, P. S., Feigelson, E. D., Townsley, L. K., et al. 2007, *ApJS*, 169, 353, doi: [10.1086/512068](https://doi.org/10.1086/512068)
- Brusa, M., Bongiorno, A., Cresci, G., et al. 2015, *MNRAS*, 446, 2394, doi: [10.1093/mnras/stu2117](https://doi.org/10.1093/mnras/stu2117)
- Buchner, J. 2021, *The Journal of Open Source Software*, 6, 3001, doi: [10.21105/joss.03001](https://doi.org/10.21105/joss.03001)
- Buchner, J., Georgakakis, A., Nandra, K., et al. 2014, *A&A*, 564, A125, doi: [10.1051/0004-6361/201322971](https://doi.org/10.1051/0004-6361/201322971)
- Corral, A., Georgantopoulos, I., Comastri, A., et al. 2016, *A&A*, 592, A109, doi: [10.1051/0004-6361/201527624](https://doi.org/10.1051/0004-6361/201527624)
- Cristello, N., Zou, F., Brandt, W. N., et al. 2024, *ApJ*, 977, 113, doi: [10.3847/1538-4357/ad8c3f](https://doi.org/10.3847/1538-4357/ad8c3f)
- de la Vega, A., Kassin, S. A., Pacifici, C., et al. 2025, *ApJ*, 980, 168, doi: [10.3847/1538-4357/ada8a2](https://doi.org/10.3847/1538-4357/ada8a2)
- Dey, A., Soifer, B. T., Desai, V., et al. 2008, *ApJ*, 677, 943, doi: [10.1086/529516](https://doi.org/10.1086/529516)
- Eisenhardt, P. R. M., Wu, J., Tsai, C.-W., et al. 2012, *ApJ*, 755, 173, doi: [10.1088/0004-637X/755/2/173](https://doi.org/10.1088/0004-637X/755/2/173)
- Fabian, A. C. 2012, *ARA&A*, 50, 455, doi: [10.1146/annurev-astro-081811-125521](https://doi.org/10.1146/annurev-astro-081811-125521)
- Fabian, A. C., Celotti, A., & Erlund, M. C. 2006, *MNRAS*, 373, L16, doi: [10.1111/j.1745-3933.2006.00234.x](https://doi.org/10.1111/j.1745-3933.2006.00234.x)

- Finnerty, L., Larson, K., Soifer, B. T., et al. 2020, *ApJ*, 905, 16, doi: [10.3847/1538-4357/abc3bf](https://doi.org/10.3847/1538-4357/abc3bf)
- Glikman, E., LaMassa, S., Piconcelli, E., Urry, M., & Lacy, M. 2017, *ApJ*, 847, 116, doi: [10.3847/1538-4357/aa88ac](https://doi.org/10.3847/1538-4357/aa88ac)
- Goulding, A. D., Zakamska, N. L., Alexandroff, R. M., et al. 2018, *ApJ*, 856, 4, doi: [10.3847/1538-4357/aab040](https://doi.org/10.3847/1538-4357/aab040)
- Hopkins, P. F., & Elvis, M. 2010, *MNRAS*, 401, 7, doi: [10.1111/j.1365-2966.2009.15643.x](https://doi.org/10.1111/j.1365-2966.2009.15643.x)
- Hopkins, P. F., Hernquist, L., Cox, T. J., et al. 2006, *ApJS*, 163, 1, doi: [10.1086/499298](https://doi.org/10.1086/499298)
- Hopkins, P. F., Hernquist, L., Cox, T. J., & Kereš, D. 2008, *ApJS*, 175, 356, doi: [10.1086/524362](https://doi.org/10.1086/524362)
- Ishibashi, W., & Fabian, A. C. 2015, *MNRAS*, 451, 93, doi: [10.1093/mnras/stv944](https://doi.org/10.1093/mnras/stv944)
- Ishibashi, W., Fabian, A. C., & Arakawa, N. 2021, *MNRAS*, 502, 3638, doi: [10.1093/mnras/stab266](https://doi.org/10.1093/mnras/stab266)
- Ishibashi, W., Fabian, A. C., Ricci, C., & Celotti, A. 2018, *MNRAS*, 479, 3335, doi: [10.1093/mnras/sty1620](https://doi.org/10.1093/mnras/sty1620)
- Jun, H. D., Assef, R. J., Bauer, F. E., et al. 2020, *ApJ*, 888, 110, doi: [10.3847/1538-4357/ab5e7b](https://doi.org/10.3847/1538-4357/ab5e7b)
- Kakkad, D., Mainieri, V., Padovani, P., et al. 2016, *A&A*, 592, A148, doi: [10.1051/0004-6361/201527968](https://doi.org/10.1051/0004-6361/201527968)
- Kayal, A., & Singh, V. 2024, *MNRAS*, 531, 830, doi: [10.1093/mnras/stae1191](https://doi.org/10.1093/mnras/stae1191)
- LaMassa, S. M., Ricarte, A., Glikman, E., et al. 2016, *ApJ*, 820, 70, doi: [10.3847/0004-637X/820/1/70](https://doi.org/10.3847/0004-637X/820/1/70)
- LaMassa, S. M., Glikman, E., Brusa, M., et al. 2017, *ApJ*, 847, 100, doi: [10.3847/1538-4357/aa87b5](https://doi.org/10.3847/1538-4357/aa87b5)
- Lansbury, G. B., Banerji, M., Fabian, A. C., & Temple, M. J. 2020, *MNRAS*, 495, 2652, doi: [10.1093/mnras/staa1220](https://doi.org/10.1093/mnras/staa1220)
- Lansbury, G. B., Gandhi, P., Alexander, D. M., et al. 2015, *ApJ*, 809, 115, doi: [10.1088/0004-637X/809/2/115](https://doi.org/10.1088/0004-637X/809/2/115)
- Lanzuisi, G., Piconcelli, E., Fiore, F., et al. 2009, *A&A*, 498, 67, doi: [10.1051/0004-6361/200811282](https://doi.org/10.1051/0004-6361/200811282)
- Li, G., Assef, R. J., Tsai, C.-W., et al. 2024, *ApJ*, 971, 40, doi: [10.3847/1538-4357/ad5317](https://doi.org/10.3847/1538-4357/ad5317)
- Martocchia, S., Piconcelli, E., Zappacosta, L., et al. 2017, *A&A*, 608, A51, doi: [10.1051/0004-6361/201731314](https://doi.org/10.1051/0004-6361/201731314)
- Mountrichas, G., Georgantopoulos, I., Secrest, N. J., et al. 2017, *MNRAS*, 468, 3042, doi: [10.1093/mnras/stx572](https://doi.org/10.1093/mnras/stx572)
- Narayanan, D., Dey, A., Hayward, C. C., et al. 2010, *MNRAS*, 407, 1701, doi: [10.1111/j.1365-2966.2010.16997.x](https://doi.org/10.1111/j.1365-2966.2010.16997.x)
- Ricci, C., Assef, R. J., Stern, D., et al. 2017a, *ApJ*, 835, 105, doi: [10.3847/1538-4357/835/1/105](https://doi.org/10.3847/1538-4357/835/1/105)
- Ricci, C., Trakhtenbrot, B., Koss, M. J., et al. 2017b, *Nature*, 549, 488, doi: [10.1038/nature23906](https://doi.org/10.1038/nature23906)
- Riguccini, L. A., Treister, E., Menéndez-Delmestre, K., et al. 2019, *AJ*, 157, 233, doi: [10.3847/1538-3881/ab16cd](https://doi.org/10.3847/1538-3881/ab16cd)
- Sanders, D. B., Soifer, B. T., Elias, J. H., et al. 1988, *ApJ*, 325, 74, doi: [10.1086/165983](https://doi.org/10.1086/165983)
- Shen, Y. 2013, *Bulletin of the Astronomical Society of India*, 41, 61, doi: [10.48550/arXiv.1302.2643](https://doi.org/10.48550/arXiv.1302.2643)
- Siemiginowska, A., Burke, D., Günther, H. M., et al. 2024, *ApJS*, 274, 43, doi: [10.3847/1538-4365/ad7bab](https://doi.org/10.3847/1538-4365/ad7bab)
- Stern, D. 2015, *ApJ*, 807, 129, doi: [10.1088/0004-637X/807/2/129](https://doi.org/10.1088/0004-637X/807/2/129)
- Stern, D., Assef, R. J., Benford, D. J., et al. 2012, *ApJ*, 753, 30, doi: [10.1088/0004-637X/753/1/30](https://doi.org/10.1088/0004-637X/753/1/30)
- Stern, D., Lansbury, G. B., Assef, R. J., et al. 2014, *ApJ*, 794, 102, doi: [10.1088/0004-637X/794/2/102](https://doi.org/10.1088/0004-637X/794/2/102)
- Toba, Y., Bae, H.-J., Nagao, T., et al. 2017, *ApJ*, 850, 140, doi: [10.3847/1538-4357/aa918a](https://doi.org/10.3847/1538-4357/aa918a)
- Toba, Y., & Nagao, T. 2016, *ApJ*, 820, 46, doi: [10.3847/0004-637X/820/1/46](https://doi.org/10.3847/0004-637X/820/1/46)
- Toba, Y., Yamada, S., Ueda, Y., et al. 2020, *ApJ*, 888, 8, doi: [10.3847/1538-4357/ab5718](https://doi.org/10.3847/1538-4357/ab5718)
- Treister, E., Natarajan, P., Sanders, D. B., et al. 2010, *Science*, 328, 600, doi: [10.1126/science.1184246](https://doi.org/10.1126/science.1184246)
- Tsai, C.-W., Eisenhardt, P. R. M., Wu, J., et al. 2015, *ApJ*, 805, 90, doi: [10.1088/0004-637X/805/2/90](https://doi.org/10.1088/0004-637X/805/2/90)
- Tsai, C.-W., Eisenhardt, P. R. M., Jun, H. D., et al. 2018, *ApJ*, 868, 15, doi: [10.3847/1538-4357/aae698](https://doi.org/10.3847/1538-4357/aae698)
- Urrutia, T., Lacy, M., Gregg, M. D., & Becker, R. H. 2005, *ApJ*, 627, 75, doi: [10.1086/430165](https://doi.org/10.1086/430165)
- Vito, F., Brandt, W. N., Stern, D., et al. 2018, *MNRAS*, 474, 4528, doi: [10.1093/mnras/stx3120](https://doi.org/10.1093/mnras/stx3120)
- Weisskopf, M. C., Wu, K., Trimble, V., et al. 2007, *ApJ*, 657, 1026, doi: [10.1086/510776](https://doi.org/10.1086/510776)
- Wu, J., Tsai, C.-W., Sayers, J., et al. 2012, *ApJ*, 756, 96, doi: [10.1088/0004-637X/756/1/96](https://doi.org/10.1088/0004-637X/756/1/96)
- Wu, J., Jun, H. D., Assef, R. J., et al. 2018, *ApJ*, 852, 96, doi: [10.3847/1538-4357/aa9ff3](https://doi.org/10.3847/1538-4357/aa9ff3)
- Yu, Z., Brandt, W. N., Zou, F., et al. 2024, *ApJ*, 977, 210, doi: [10.3847/1538-4357/ad8bc0](https://doi.org/10.3847/1538-4357/ad8bc0)
- Zappacosta, L., Piconcelli, E., Duras, F., et al. 2018, *A&A*, 618, A28, doi: [10.1051/0004-6361/201732557](https://doi.org/10.1051/0004-6361/201732557)
- Zou, F., Brandt, W. N., Vito, F., et al. 2020, *MNRAS*, 499, 1823, doi: [10.1093/mnras/staa2930](https://doi.org/10.1093/mnras/staa2930)